Available online at www.sciencedirect.com
SCIENCE DIRECT®
International Journal of Solids and Structures 43 (2006) 4238–4257
INTERNATIONAL JOURNAL OF SOLIDS and STRUCTURES
www.elsevier.com/locate/ijsolstr

Damage estimation on beam-like structures using the multi-resolution analysis

Byeong Hwa Kim [a], Taehyo Park [b], George Z. Voyiadjis [c,*]

[a] *Computational Solid and Structural Mechanics Lab., Department of Civil Engineering, Hanyang University, 17 Haengdang-dong, Seoul 133-791, Republic of Korea*
[b] *Department of Civil Engineering, Hanyang University, 17 Haengdang-dong, Seoul 133-791, Republic of Korea*
[c] *Department of Civil and Environmental Engineering, Louisiana State University, Baton Rouge, LA 70803, USA*

Received 3 March 2005
Available online 8 September 2005

Abstract

This work proposes a vibration-based damage evaluation method that can detect, locate, and size damage utilizing only a few of the lower mode shapes. The proposed method is particularly advantageous for beam-like structures with uncertain applied axial load, mass density, and foundation stiffness. Based on a small damage assumption, a linear relationship between damaged and undamaged curvatures is revealed in the context of elasticity. It turns out that the resulting damage index equation inherently suffers from singularities near inflection nodes. The transformation of the problem into the multi-resolution wavelet domain provides a set of coupled linear equations. With the aid of the singular value decomposition technique, the solution to the damage index equation is achieved in the wavelet space. Next, the desired physical solution to the damage index equation is reconstructed from the one in the wavelet space. The performance of the proposed method is compared with two existing damage detection methods using a set of numerical simulations. The proposed method attempts to resolve the mode selection problem, the singularity problem, the axial force problem, and the absolute severity estimation problem, all of which remained unsolved by earlier attempts.
© 2005 Elsevier Ltd. All rights reserved.

Keywords: Damage detection; Multi-resolution analysis; Wavelet applications; Curvature of mode shape; Haar wavelet; Singular value decomposition; Beam column

* Corresponding author.
E-mail address: voyiadjis@eng.lsu.edu (G.Z. Voyiadjis).

0020-7683/$ - see front matter © 2005 Elsevier Ltd. All rights reserved.
doi:10.1016/j.ijsolstr.2005.07.022

1. Introduction

It is essential to periodically monitor the load-carrying capacity of a structure, since the accumulation of damage may result in a catastrophic structural failure. For such an application, the vibration-based inspection method has received increasing attention for civil engineering structures. This is due to remarkable advances in techniques for the extraction of modal parameters of real structures. However, the vibration-based nondestructive damage evaluation (NDE) techniques inherently suffer from the following incompleteness of measured modal data: (1) only a few of the lower modes can be measured; (2) the complete sets of degrees of freedom cannot be measured; and (3) the complete spatial resolution of mode shape cannot be achieved. Attempts to overcome this incompleteness of measured modal data have motivated the continued evolution of NDE techniques over the last two decades.

Damage in a structure may cause various changes in structural responses such as frequency shifts, mode shape variations, changes in mode shape curvature, changes in modal flexibility, variations in strain mode shape, modal strain energy fluctuations, etc. Among the various research efforts, the utilization of a frequency shift was popular in early studies. The frequency-based NDE is based on the concept that changes in local stiffness are reflected by changes in eigen-frequencies (Cawley and Adams, 1979). The apparent practical advantage using natural frequencies for NDE is twofold: First, frequency information is independent of the probing position of the transducers; second, the measured frequencies are relatively accurate compared to mode shapes. Consequently, several techniques have been proposed to detect, locate, and size damage using frequency information. However, the frequency-based methods have at least two weaknesses: First, the frequencies of structures are also affected by changes in mass density, applied axial force, and foundation stiffness. In practice, such structural changes are generally unknown. Furthermore, the natural frequencies are altered by the site's environmental conditions such as air temperature, humidity, mean air pressure, and rainfall on the day preceding the test (Farrar and Jauregui, 1998). In addition, in the case of symmetrical structures, the changes in natural frequency due to damage at two symmetric locations are exactly the same. Thus, solutions may not be unique. Second, in the case of small, local damage, frequency changes could be comparable in size to the measurement errors. Thus, the insensitivity problem is unavoidable in frequency-based methods.

Such drawbacks of the frequency approaches draw special attention to methods utilizing displacement measures such as the mode shape curvature (MSC) method given by Pandey et al. (1991) and the damage index (DI) method given by Stubbs et al. (1995). Simulating damage on a cantilever and a simply supported beam model, Pandey et al. (1991) numerically showed that the changes in the curvature mode shapes are highly sensitive to damage and can be used to localize it. The MSC method utilizes the flexural formula for an Euler–Bernoulli beam, and the curvatures of mode shapes are obtained by applying the central difference formula to the measured mode shapes. However, the MSC method has at least the following five deficiencies: First, the small errors in mode shape measurements may be magnified in the required central difference process. Second, the method requires a sufficient spatial resolution to obtain accurate second derivatives of mode shapes. Third, the estimation results can be different if more than one mode is used. Fourth, the method cannot estimate the absolute severity of damage even when the localization of damage is successful. Finally, the singularity problems near the inflection points of mode shapes make detecting damage more difficult.

The first weakness is unavoidable, because the MSC method is based on the displacement measures. Compared to the second weakness of the frequency-based methods, this trade-off is essential for higher sensitivity to damage. In general, the intensity of this problem can significantly be reduced by a large number of statistical tests. Another approach to resolve this problem is to use wavelets. The concept behind applying wavelets is that the wavelet transformation with n vanishing moments is identical to differencing the signal n times (Shao and Ma, 2003). Thus, the finite difference process to obtain the second derivative of mode shapes could be replaced by the wavelet transformation. Recently, wavelets with two vanishing

moments have been applied for damage detection (Wang and Deng, 1999; Hong et al., 2002; Douka et al., 2003; Gentile and Messina, 2003; Messina, 2004; Loutridis et al., 2004). In such applications, the Haar wavelet among the various wavelets is excluded because it has vanishing moments of first order. The apparent advantage of the wavelet application lies only in its de-noising feature. However, this limitation of the wavelet technique is shared with the mentioned second through fourth limitations of the MSC method. The second shortcoming of the MSC method can be overcome by increasing the number of measurement locations. Although this requirement may not be acceptable for a conventional transducer, a recently developed scanning laser vibrometer could make it feasible. In the technical literature, the feasibility studies on the use of a large number measurement grid with a large number of sampling points have been reported and have been accepted recently by several pioneers. For instance, Pai and Young (2001) have reported the successful collection of the operational deflection shapes at 200 or 400 points for both a real beam and plate using a scanning laser vibrometer. To date, the third, fourth, and fifth shortcomings listed may be critical, because there is no way to resolve such problems even at cost. A few attempts to resolve those problems have been reported. To resolve the third shortcoming, Doebling et al. (1996) and Pandey et al. (1994) suggest the use of modal flexibility, because it provides a rational way to combine all the measured modes. However, the modal flexibility still depends on mass and surrounding stress, because it is reconstructed from frequency information. To resolve the fourth drawback, Wahab and Roeck (1999) propose a curvature damage factor. However, no theoretical support for the proposed indicator has yet been presented. As a consequence, the proposed factor still shares the same difficulty. To resolve the fifth drawback, Kim et al. (2002) derived the so-called flexural damage index equation. However, the proposed approach does not consider the nonlinearity due to an axial force and mass uncertainty because of the utilization of modal flexibility. Therefore, the third, fourth, and fifth drawbacks of the family of MSC methods *still need to be addressed.*

This study attempts to overcome the aforementioned drawbacks, and to improve the efficiency, accuracy, and reliability of the family of MSC methods. To achieve this objective, we follow three steps: First, the theoretical background of damage mechanics and the fundamentals of multi-resolution Haar wavelet transformations is discussed in detail. Second, with the aid of the wavelet transformation, a technique for solving the previously derived damage index equation is introduced. Finally, various numerical verifications are provided to illustrate the performance of the proposed approach.

2. A theory of damage detection

2.1. Damage mechanics

Consider a deformable body shown in Fig. 1. The real line, w, denotes a deformed configuration with an elastic modulus E due to the applied loads (P_1, P_2, and P_3). The dashed line, w^*, denotes a deformed configuration due to changes in the elastic modulus of E^* at an arbitrary location. Assume that the presence of the small deformations (δ_1, δ_2, and δ_3) due to damage and slight changes in the lines of action of the loads will have only an insignificant effect on the internal forces. This condition requires that the change in shapes of the body due to damage must not affect the action of the applied loads. In the development that follows, two conditions are assumed to hold. First, a small damage event, a priori, will have no effect on the internal forces of a statically determinate structure. Second, it is assumed that the same condition holds in a statically indeterminate structure with low redundancy. Hence, the stresses, σ, in the deformable configuration are constant during changes in strain due to damage:

$$\sigma = \sigma^* \tag{1}$$

where the asterisk denotes the damaged state. The stress-strain relationship of a deformable body following Hook's law is illustrated in Fig. 2. The strain energy densities before and after a small damage event are the

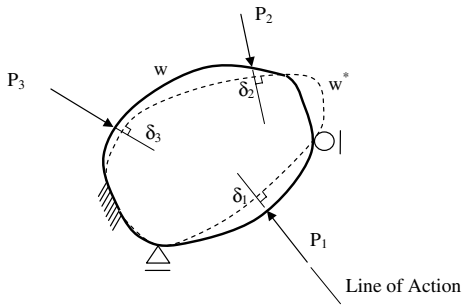

Fig. 1. Deformed configurations.

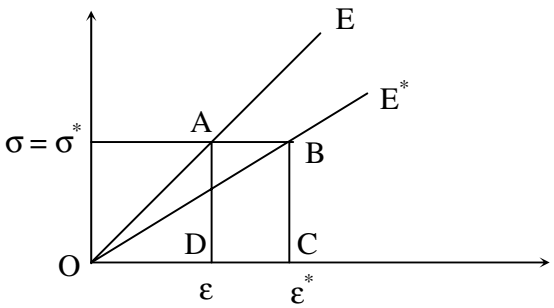

Fig. 2. Stress strain changes due to damage.

areas OAD and OBC, respectively. Thus, total strain energy is altered by damage during a small damage event. The work done on stress fibers caused by a preloading is the area ABCD. Hence, the strain energy density supplied to the body for the damage event is equal to the area OAD + ABCD − OBC = OAB.

In the case of the Euler–Bernoulli beam, the internal moment of a beam can be obtained by integrating Eq. (1) with respect to the cross-sectional area after multiplying by vertical coordinates on both sides:

$$M = M^* \tag{2}$$

Applying the kinematics between strain and deflection yields a damage index equation that gives a linear relationship between undamaged and damaged curvature:

$$\kappa^* = \beta\kappa \tag{3}$$

in which

$$\beta = \frac{E}{E^*} \tag{4}$$

where β and κ denote the damage index and the undamaged curvature, respectively. Suppose that the curvatures of the damaged and undamaged conditions are available. Then, the desired damage index can easily be obtained by dividing the damaged curvature by the undamaged curvature in Eq. (3) unless the undamaged curvature is nonzero.

$$\beta = \frac{\kappa^*}{\kappa} \tag{5}$$

However, inflection points of a deflection profile are often encountered in practice. Therefore, one must resort to a way of avoiding this singularity problem. To extend the generosity of solving the singularity problem, the recent application of wavelets to engineering problems draws special attention. Before discussing further developments in the damage detection theory, the following section describes the basics of the multi-resolution wavelet analysis.

2.2. Multi-resolution analysis of the Haar wavelet

The Haar basis is the simplest orthonormal wavelet basis for multi-resolution analysis (Mallat, 1998). The Haar domain consists of a scaling function $\phi(x)$ and a wavelet function $\psi(x)$. The Haar scaling function and wavelet function satisfy the following dilation and wavelet equations, respectively:

$$\phi(x) = \phi(2x) + \phi(2x-1) \tag{6}$$

$$\psi(x) = \phi(2x) - \phi(2x-1) \tag{7}$$

Multiplying both sides by a factor 1/2, Eqs. (6) and (7) reveal that the scaling and wavelet functions act like averaging and differencing operators, respectively (Stollnitz et al., 1995). The solutions to the scaling and wavelet equation are known as:

$$\phi(x) = \begin{cases} 1, & 0 \leqslant x < 1 \\ 0, & \text{otherwise} \end{cases} \tag{8}$$

$$\psi(x) = \begin{cases} 1, & 0 \leqslant x < 1/2 \\ -1, & 1/2 \leqslant x < 1 \\ 0, & \text{otherwise} \end{cases} \tag{9}$$

Plots of the scaling and wavelet equations are given in Fig. 3.

Consider functions defined on the interval $0 \leqslant x < 1$. Let $\mathbf{V}_j$ be a set of functions that are constant on the 2^j intervals $\{n/2^j \leqslant x < (n+1)/2^j, n = 0, 1, \ldots, 2^j - 1\}$. Then, any function in $\mathbf{V}_j$ can be represented by a linear combination of the 2^j orthonormal functions:

$$\phi_{j,n}(x) \equiv 2^{j/2}\phi(2^j x - n) \tag{10}$$

$$\psi_{j,n}(x) \equiv 2^{j/2}\psi(2^j x - n) \tag{11}$$

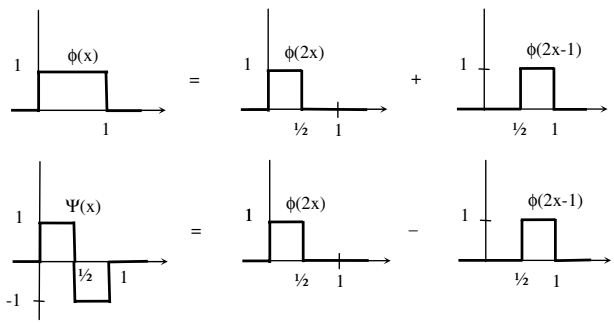

Fig. 3. Scaling and wavelet equation of Haar basis.

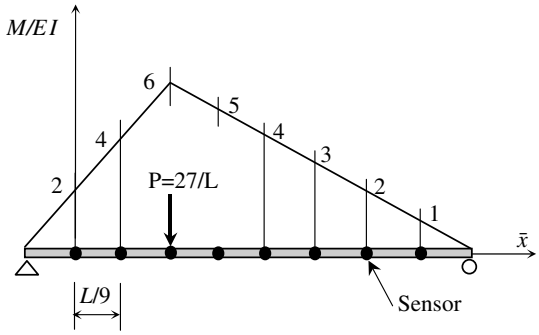

Fig. 4. Curvature profile caused by applied load.

The factor $2^{j/2}$ only plays a role in the normalization of $\phi(2^j x - n)$, since $\int[\phi(2^{j/2}x)]^2 \mathrm{d}x = 2^{-j}$. For a fixed resolution level j, the scaling and wavelet bases are defined by

$$\mathbf{\Phi}_j = \left\{\phi_{j,n}(x),\ n = 0, 1, \ldots, 2^j - 1\right\} \tag{12}$$

$$\mathbf{\Psi}_j = \left\{\psi_{j,n}(x),\ n = 0, 1, \ldots, 2^j - 1\right\} \tag{13}$$

Applying Eqs. (6) and (7), the basis of $\mathbf{\Phi}_j$ can be represented by a direct sum of two orthonormal bases of the next lower resolution level:

$$\mathbf{\Phi}_j = \mathbf{\Phi}_{j-1} \oplus \mathbf{\Psi}_{j-1} \tag{14}$$

Let the space $\mathbf{V}_j$ be represented by $\mathbf{\Phi}_j$. Then the successive application of Eq. (14) yields

$$\mathbf{V}_j = \mathbf{\Phi}_0 \oplus \mathbf{\Psi}_0 \oplus \mathbf{\Psi}_1 \oplus \mathbf{\Psi}_2 \oplus \cdots \oplus \mathbf{\Psi}_{j-2} \oplus \mathbf{\Psi}_{j-1} \tag{15}$$

Therefore, any function in $\mathbf{V}_j$ can be represented by a set of wavelet bases $\mathbf{\Psi}_j$ and a fundamental scale basis $\mathbf{\Phi}_0$.

For instance, consider a simply supported beam with total length L. For a transverse load $P = 27/L$, the curvature profile measured at the 8 nodes with a uniform interval of $L/9$ is shown in Fig. 4. For a nondimensional coordinate, $x = \bar{x}/L$ starting from the first sensor location, the resolution level of the measured curvature profile, $\kappa = \{2, 4, 6, 5, 4, 3, 2, 1\}$, becomes at least $j = 3$ because $2^j = 8$. The curvature profile sequences can be represented by a linear combination of the $2^3 = 8$ scaling functions $\phi_{3,n}(x) = 2^{3/2}\phi(2^3 x - n)$, $n = \{0, 1, \ldots, 7\}$:

$$\kappa(x) = \sum_{n=0}^{7} a_{3,n}\phi_{3,n}(x) \tag{16}$$

where $a_{j,n}$ denotes the nth representation of $\kappa(x)$ in the space $\mathbf{\Phi}_j$. Applying the inner product to $\kappa(x)$ and $\phi_{3,n}(x)$, the representation coefficients can easily be extracted: $a_3 = 2^{-3/2}\{2, 4, 6, 5, 4, 3, 2, 1\}$. The next step involves finding the scaling and wavelet functions at the resolution level $j = 2$. Note that the space $\mathbf{\Phi}_3$ can be decomposed into two subspaces, $\mathbf{\Phi}_2$ and $\mathbf{\Psi}_2$, whose bases consist of the functions $\phi_{2,n}(x) = \phi(2^2 x - n)$ and $\psi_{2,n}(x) = \psi(2^2 x - n)$ for $n = \{0, 1, \ldots, 3\}$, respectively. Therefore, the curvature can be expressed by

$$\kappa(x) = \sum_{n=0}^{3} a_{2,n}\phi_{2,n}(x) + \sum_{n=0}^{3} b_{2,n}\psi_{2,n}(x) \tag{17}$$

where $b_{j,n}$ denotes the nth representation of $\kappa(x)$ in the space $\mathbf{\Psi}_j$. Combining Eqs. (16) and (17) yields

$$\sum_{n=0}^{7} a_{3,n}\phi_{3,n}(x) = \sum_{n=0}^{3} a_{2,n}\phi_{2,n}(x) + \sum_{n=0}^{3} b_{2,n}\psi_{2,n}(x) \tag{18}$$

After multiplying both sides of Eq. (18) by $\phi_{2,n}(x)$, and integrating with respect to x yields the representations of $a_{2,n}$:

$$a_{2,n} = 2^{-1/2}(a_{3,2n} + a_{3,2n+1}) \quad \text{for } n = \{0, 1, \ldots, 3\} \tag{19}$$

Note that the orthonormal condition between the spaces $\mathbf{\Phi}_2$ and $\mathbf{\Psi}_2$ makes the manipulation easy. Similarly, the representation $b_{2,n}$ can be obtained by the integration after multiplying both sides of Eq. (18) by $\psi_{2,n}(x)$:

$$b_{2,n} = 2^{-1/2}(a_{3,2n} - a_{3,2n+1}) \quad \text{for } n = \{0, 1, \ldots, 3\} \tag{20}$$

The explicit expressions of the resulting representations for the resolution level 2 are $a_2 = 2^{-2}\{6, 11, 7, 3\}$ and $b_2 = 2^{-2}\{-2, 1, 1, 1\}$. By the same token, the space $\mathbf{\Phi}_2$ can be further decomposed into two subspaces, $\mathbf{\Phi}_1$ and $\mathbf{\Psi}_1$, whose basis components consist of $\phi_{1,n}(x) = 2^{1/2}\phi(2x - n)$ and $\psi_{1,n}(x) = 2^{1/2}\psi(2x - n)$ for $n = \{0, 1\}$, respectively. Then, the first term in the right hand side of Eq. (18) can be written as

$$\sum_{n=0}^{3} a_{2,n}\phi_{2,n}(x) = \sum_{n=0}^{1} a_{1,n}\phi_{1,n}(x) + \sum_{n=0}^{1} b_{1,n}\psi_{1,n}(x) \tag{21}$$

The identical procedure using the orthonormal property in the resolution level $j = 1$ yields the unknown representations:

$$a_{1,n} = 2^{-1/2}(a_{2,2n} + a_{2,2n+1}) \quad \text{for } n = \{0, 1\} \tag{22}$$

$$b_{1,n} = 2^{-1/2}(a_{2,2n} - a_{2,2n+1}) \quad \text{for } n = \{0, 1\} \tag{23}$$

After some calculations, we then obtain $a_1 = 2^{-5/2}\{17, 10\}$ and $b_1 = 2^{-5/2}\{-5, 4\}$. Similarly, the space $\mathbf{\Phi}_1$ can be decomposed into two subspaces, $\mathbf{\Phi}_0$ and $\mathbf{\Psi}_0$. The first term in the right hand side of Eq. (21) can be written as

$$\sum_{n=0}^{1} a_{1,n}\phi_{1,n}(x) = \sum_{n=0}^{0} a_{0,n}\phi_{0,n}(x) + \sum_{n=0}^{0} b_{0,n}\psi_{0,n}(x) \tag{24}$$

where $a_{0,0} = \frac{27}{8}$ and $b_{0,0} = \frac{7}{8}$. Combining Eq. (17) with Eqs. (21) and (24) yields the curvature in terms of wavelet basis:

$$\kappa(x) = \sum_{n=0}^{0} a_{0,0}\phi_{0,n}(x) + \sum_{n=0}^{0} b_{0,n}\psi_{0,n}(x) + \sum_{n=0}^{1} b_{1,n}\psi_{1,n}(x) + \sum_{n=0}^{3} b_{2,n}\psi_{2,n}(x) \tag{25}$$

Note that the curvature in terms of the scaling function at a single resolution level $j = 3$ (see Eq. (16)) is now expressed by the wavelet functions at multiple resolution levels in Eq. (25). This iterative, hierarchical successive decomposition procedure is called the multi-resolution analysis of wavelets. Eq. (25) is illustrated in Fig. 5. Hence, the representation of the curvature in the Haar wavelet basis is $\kappa_{\text{Haar}} = \left\{\frac{27}{8}, \frac{7}{8}, -\frac{5}{4\sqrt{2}}, \frac{1}{\sqrt{2}}, -\frac{1}{2}, \frac{1}{4}, \frac{1}{4}, \frac{1}{4}\right\}$. Note that the representation $a_{0,0}$ is equal to the average value of all

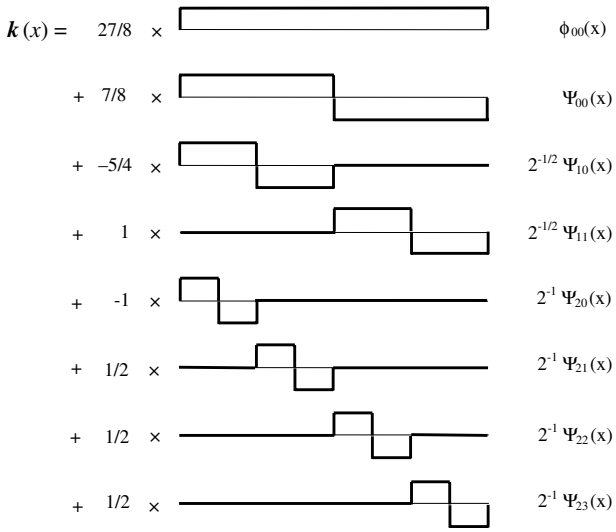

Fig. 5. Haar representations of the curvature profile.

the measured curvatures. Furthermore, a set of multi-resolution wavelet bases and a scaling basis comprise a set of orthonormal bases (see Eq. (15)) although the scaling bases are not orthogonal for each resolution level.

The Haar wavelet basis has many features. One important feature is the capability for coupling with only a finite number of adjacent data points. For instance, the Haar transformation of a unit impulse $\{1,0,0,0,0,0,0,0\}$ is $\left\{\frac{1}{8},\frac{1}{8},\frac{1}{4\sqrt{2}},0,\frac{1}{4},0,0,0\right\}$. Unlike the Fourier basis, the unit impulse is correlated with four nonzero values in the Haar basis. Therefore, a point-wise relation in the real domain can be transformed into the finite coupling one in the Haar domain. As shown in the following section, this feature plays a major role in resolving the singularity problem in Eq. (3).

2.3. Damage evaluation using multi-resolution wavelet analysis

For the resolution level j, the curvature profiles in Eq. (25) can be rewritten as

$$\kappa(x) = a_{0,0}\phi_{0,0}(x) + \sum_{m=0}^{j-1}\sum_{n=0}^{2^m-1} b_{m,n}\psi_{m,n}(x) \tag{26}$$

Now, the damaged curvature profiles $\kappa^*(x)$ and the damage index $\beta(x)$ can be also represented by the same multi-resolution wavelet basis:

$$\kappa^*(x) = a^*_{0,0}\phi_{0,0}(x) + \sum_{m=0}^{j-1}\sum_{n=0}^{2^m-1} b^*_{m,n}\psi_{m,n}(x) \tag{27}$$

$$\beta(x) = p_{0,0}\phi_{0,0}(x) + \sum_{m=0}^{j-1}\sum_{n=0}^{2^m-1} q_{m,n}\psi_{m,n}(x) \tag{28}$$

where $p_{0,0}$ and $q_{m,n}$ are the 0th and nth representation of the function $\beta(x)$ in the space $\mathbf{\Phi}_0$ and $\mathbf{\Psi}_m$, respectively. Substituting Eqs. (26)–(28) into the previously derived damage index equation (3) yields

$$a^*_{0,0}\phi_{0,0}(x) + \sum_{m=0}^{j-1}\sum_{n=0}^{2^m-1} b^*_{m,n}\psi_{m,n}(x) = p_{0,0}\left(a_{0,0}\phi^2_{0,0}(x) + \sum_{m=0}^{j-1}\sum_{n=0}^{2^m-1} b_{m,n}\psi_{m,n}(x)\phi_{0,0}(x)\right) + \sum_{m=0}^{j-1}\sum_{n=0}^{2^m-1} q_{m,n}\left(a_{0,0}\phi_{0,0}(x)\psi_{m,n}(x) + \sum_{k=0}^{j-1}\sum_{t=0}^{2^k-1} b_{m,n}\psi_{m,n}(x)\psi_{k,t}(x)\right) \quad (29)$$

Suppose that the representations $\{a_{0,0}, b_{m,n}, a^*_{0,0}, b^*_{m,n}\}$ of the measured curvatures in the damaged and undamaged conditions are known by the Haar transformation. Then, the representations $\{p_{0,0}, q_{m,n}\}$ of the damage index $\beta(x)$ can be identified. After multiplying both sides of Eq. (29) by $\phi_{0,0}(x)$, the integration with respect to x from zero to unity yields:

$$a^*_{0,0} = p_{0,0}a_{0,0} + q_{0,0}b_{0,0} + q_{1,0}b_{1,0} + q_{1,1}b_{1,1} + \cdots q_{j-1,2^{j-1}-1}b_{j-1,2^{j-1}-1} \quad (30)$$

Note that the orthonormal property of the multi-resolution wavelet basis plays a significant role in reducing computation. Similarly, the integration after multiplication of $\phi_{m,n}(x)$ into Eq. (29) yields:

$$\begin{aligned} b^*_{m,n} = {} & q_{0,0}\left(a_{0,0}\int_0^1 \phi_{0,0}\phi_{0,0}\phi_{m,n}\,\mathrm{d}x + \sum_{k=0}^{j-1}\sum_{t=0}^{2^k-1} b_{k,t}\int_0^1 \phi_{0,0}\psi_{k,t}\phi_{m,n}\,\mathrm{d}x\right) \\ & + q_{1,0}\left(a_{0,0}\int_0^1 \psi_{1,0}\phi_{0,0}\phi_{m,n}\,\mathrm{d}x + \sum_{k=0}^{j-1}\sum_{t=0}^{2^k-1} b_{k,t}\int_0^1 \psi_{1,0}\psi_{k,t}\phi_{m,n}\,\mathrm{d}x\right) \\ & + q_{1,1}\left(a_{0,0}\int_0^1 \psi_{1,1}\phi_{0,0}\phi_{m,n}\,\mathrm{d}x + \sum_{k=0}^{j-1}\sum_{t=0}^{2^k-1} b_{k,t}\int_0^1 \psi_{1,1}\psi_{k,t}\phi_{m,n}\,\mathrm{d}x\right)\cdots \\ & + q_{j-1,2^{j-1}-1}\left(a_{0,0}\int_0^1 \psi_{j-1,2^{j-1}-1}\phi_{0,0}\phi_{m,n}\,\mathrm{d}x + \sum_{k=0}^{j-1}\sum_{t=0}^{2^k-1} b_{k,t}\int_0^1 \psi_{j-1,2^{j-1}-1}\psi_{k,t}\phi_{m,n}\,\mathrm{d}x\right) \end{aligned} \quad (31)$$

Combining Eqs. (30) and (31) yields a set of coupled linear algebraic matrix equations:

$$\mathbf{Ax} = \mathbf{b} \quad (32)$$

where the $j \times 1$ vector $\mathbf{x} = \lfloor p_{0,0}, q_{0,0}, q_{1,0}, q_{1,1}, q_{2,0}, \ldots, q_{j-1,2^{j-1}-1}\rfloor^{\mathrm{T}}$ denotes the representation coefficients of the damage indices to be identified. The $j \times 1$ vector $\mathbf{b} = [a^*_{0,0}, b^*_{0,0}, \ldots, b^*_{j-1,2^{j-1}-1}]^{\mathrm{T}}$ denotes the representations of the damaged curvature in the Haar basis. The $j \times j$ matrix $\mathbf{A}$ denotes the brackets in Eq. (31). When computing the matrix $\mathbf{A}$, the direct numerical integration of the three multiples of the basis function is not recommended. One can easily obtain the matrix $\mathbf{A}$ by simple multiplications and summation of the Haar basis functions because they are constants in their support. In principle, any wavelet can be used to construct Eq. (32). However, the Haar wavelet is the best for the computation of the required triple integral in Eq. (31). If there is no singularity in the curvature, the solution can be easily achieved by solving Eq. (32) for the representations of damage index. Using the resulting representations of damage index in the Haar domain, the physical true damage index can be reconstructed by Eq. (28).

For instance, consider a damaged curvature profile $\kappa^* = \{2, 4, 6, 10, 4, 3, 2, 1\}$ caused by the 50% reduction of the flexural rigidity at the location of the 4th sensor. Using the identical multi-resolution analysis, the representations of the damaged curvature profile in the Haar domain become $\kappa^*_{\mathrm{Haar}} = \left\{4, \frac{3}{2}, -\frac{5}{2\sqrt{2}}, \frac{1}{\sqrt{2}}, -\frac{1}{2}, -1, \frac{1}{4}, \frac{1}{4}\right\}$. Then, the damage index equation (32) is given by

$$\begin{bmatrix} \frac{27}{8} & \frac{7}{8} & -\frac{5\sqrt{2}}{8} & \frac{1}{\sqrt{2}} & -\frac{1}{2} & \frac{1}{4} & \frac{1}{4} & \frac{1}{4} \\ \frac{7}{8} & \frac{27}{8} & -\frac{5\sqrt{2}}{8} & -\frac{1}{\sqrt{2}} & -\frac{1}{2} & \frac{1}{4} & -\frac{1}{4} & -\frac{1}{4} \\ -\frac{5\sqrt{2}}{8} & -\frac{5\sqrt{2}}{8} & \frac{17}{8} & 0 & -\frac{1}{\sqrt{2}} & -\frac{1}{2\sqrt{2}} & 0 & 0 \\ \frac{1}{\sqrt{2}} & -\frac{1}{\sqrt{2}} & 0 & \frac{5}{2} & 0 & 0 & \frac{1}{2\sqrt{2}} & -\frac{1}{2\sqrt{2}} \\ -\frac{1}{2} & -\frac{1}{2} & -\frac{1}{\sqrt{2}} & 0 & 3 & 0 & 0 & 0 \\ \frac{1}{4} & \frac{1}{4} & -\frac{1}{2\sqrt{2}} & 0 & 0 & \frac{11}{2} & 0 & 0 \\ \frac{1}{4} & -\frac{1}{4} & 0 & \frac{1}{2\sqrt{2}} & 0 & 0 & \frac{7}{2} & 0 \\ \frac{1}{4} & -\frac{1}{4} & 0 & -\frac{1}{2\sqrt{2}} & 0 & 0 & 0 & \frac{3}{2} \end{bmatrix} \begin{bmatrix} p_{0,0} \\ q_{0,0} \\ q_{1,0} \\ q_{1,1} \\ q_{2,0} \\ q_{2,1} \\ q_{2,2} \\ q_{2,3} \end{bmatrix} = \begin{bmatrix} 4 \\ \frac{3}{2} \\ -\frac{5}{2\sqrt{2}} \\ \frac{1}{\sqrt{2}} \\ -\frac{1}{2} \\ -1 \\ \frac{1}{4} \\ \frac{1}{4} \end{bmatrix} \tag{33}$$

Note that the matrix **A** is symmetric, which can reduce computational efforts significantly. Inverting the matrix **A** directly, the solution to Eq. (33) is given by $\mathbf{x} = \left\lfloor \frac{9}{8}, \frac{1}{9}, -\frac{1}{4\sqrt{2}}, 0, 0, -\frac{1}{4}, 0, 0 \right\rfloor^{\mathrm{T}}$. From this resulting representation of damaged indices in Haar wavelet domain, the desired physical damage index can be reconstructed by Eq. (28): The computed damage index is $\beta = \{1, 1, 1, 2, 1, ,1, 1, 1\}$. This result can be immediately interpreted as a 50% reduction of the Young's modulus at the location of the 4th sensor. Indeed, dividing each component of the damaged curvature profile κ^* by that of the undamaged curvature profile κ yields the exact damage indices as stated in Eq. (5). However, when the curvature profiles include zeros, one cannot apply Eq. (5) directly. In that case, the wavelet damage index equation (32) must be solved. The following section deals with such a singularity problem.

2.4. Solution to the singularity problem

If there exist r singularities in a curvature profile, the matrix **A** definitely suffers from a rank deficiency of r. Consequently, the direct inversion of the matrix **A** is not possible. This singularity problem can easily be resolved by providing the additional equations generated by the different curvature profiles. Here, a necessary condition for such an additional curvature profile is that the locations of the singularities should not the same as those in the previously used curvature profiles. In practice, a few of the lower mode shapes are available through typical modal testing. Therefore, one choice is to make use of two curvature profiles computed by the first and second mode shapes because the singularities of those profiles usually do not coincide. The other choice is to take a set of modal flexibilities reconstructed with a few lower modal parameters. Recall that modal flexibility is a modal approximation of the deflection profiles caused by a unit load (Berman and Flannelly, 1971). Thus, for a given set of modal parameters, many different deflection profiles can be reconstructed for various locations of an applied unit load. However, the modal flexibility is not free from uncertainty in mass and surrounding stresses, because the frequencies are involved in the required reconstruction process. Hence, the utilization of modal flexibility profiles is limited.

Using either curvature mode shapes or modal flexibility curvatures, the size of the matrix **A** will be increased to $m \times n$ with the condition $m > n$. Consequently, Eq. (32) results in an over-determined equation

with rank n. In this case, the a *pseudo-inverse* solution satisfying all the Moore–Penrose conditions (Golub and Van Loan, 1996) can be obtained by

$$\mathbf{x} = \mathbf{Y}\mathbf{\Omega}^{-1}\mathbf{Y}^{\mathrm{T}}\mathbf{A}^{\mathrm{T}}\mathbf{b} \tag{34}$$

where the $n \times m$ matrix $\mathbf{Y}$ and the $m \times m$ matrix $\mathbf{\Omega}$ are the sets of the singular vectors and the singular values of an $\boldsymbol{n} \times \boldsymbol{n}$ symmetric matrix $\mathbf{A}^{\mathrm{T}}\mathbf{A}$, respectively:

$$\mathbf{A}^{\mathrm{T}}\mathbf{A} = \mathbf{Y}\mathbf{\Omega}\mathbf{Y}^{\mathrm{T}} \tag{35}$$

It can be shown that the solution presented in Eq. (34) is an optimum solution of L_2 minimization. After obtaining the representations of the damage index in Eq. (34), the desired damage index can be reconstructed by Eq. (28).

2.5. Extraction of curvature profiles

In practice, the number of sensor locations is often not a power of two. To resolve this problem, one convenient choice is to add zeros. For example, if there are 14 sensors, two zeros can be added to give a total of the 16 points on mode shapes. This addition of zeros does not affect the accuracy of the estimation results.

To extract curvature profiles from mode shapes with coarse and irregular intervals, the interpolation process with a refined uniform interval is a prerequisite before differencing. The reason is that the well-known central difference formula is applicable to a uniform interval. Among many classes of interpolation functions, the *spline* interpolation of measured deflection profiles with a refined interval is preferred. This preference is totally based on various numerical experiences. After the interpolation of the deflection profiles, the refined curvature profiles can be obtained by the central difference approximation. This enlarged interpolated curvature profile could be used to extract curvatures at the sensor locations. Then, the size of the resulting curvature profile is the same as with the measured mode shape. However, there still exists uncertainty in the estimation of the severity of damage at unmeasured locations, since the true curvature profile between two measured adjacent nodes remains unknown. To alleviate this uncertainty, a recently used technique is to measure displacements on dense grids using a scanning laser vibrometer (Pai and Young, 2001).

An interesting recent alternative to computing curvature profiles from measured deflection profiles is to apply a wavelet transformation instead of a finite difference formula. Recall that the wavelet equation (7) acts like a difference operator. Thus, the wavelet transformation with n vanishing moments is analogous to differencing the signal n times. This approach is particularly advantageous when noise is involved in the measured deflection profiles. For extracting the second derivatives from the noise deflection profiles, the wavelet transformation with two vanishing moments provides superior accuracy to the finite difference formula (Shao and Ma, 2003; Gentile and Messina, 2003). However, this approach to wavelet transformation requires a dense measurement grid.

When using either method to extract the curvature profiles, the mode shapes of a structure should be extracted first. In extracting mode shapes from modal testing, one should be very careful because the statistical variation of mode shapes is typically larger than the other modal parameters. Thus, a large number of modal tests should be repeated to achieve an averaged mode shape with small statistical variations. If typical modal testing and analysis methods are used with a large number of sensor locations, the required tasks are significantly magnified. This problem can be dealt with the recently developed time domain decomposition technique (Kim et al., 2004), which is an efficient modal parameter extraction method when there are many senor locations.

3. Numerical study

For a simply supported beam, the effect of an axial force P (positive for compression), on the ith eigenvalue of the structure is (Timoshenko, 1928):

$$\omega_i^2 = \left(\frac{i\pi}{L}\right)^4 \frac{EI}{\rho A} - \left(\frac{i\pi}{L}\right)^2 \frac{P}{\rho A} \tag{36}$$

where, ρ, A, L, and EI denote the density, the cross-sectional area, total length, and flexural rigidity of the beam, respectively. The first term on right hand side of Eq. (36) represents the pure bending mode without an axial force, and the second term represents the axial mode of a flexible taut string. Thus, the natural frequencies can be changed by not only local variations of flexural rigidity, but also by changes in mass density and applied axial force. Therefore, detecting damage using only frequency information is very difficult in an axially loaded beam whose mass density varies. The mode shapes of the pinned–pinned, pinned–sliding, and sliding–sliding beam are unaffected by the applied axial force (Blevins, 1979). The mode shapes of the other boundary conditions are functions of axial load. However, the changes in mode shapes due to large changes in axial loads are generally very small.

In order to examine the performance of the proposed method, the clamped–pinned pre-stressed concrete beam in Fig. 6 was considered. The sectional area, second moment of area, Young's modulus, length, and density of the beam, were 0.11 m^2, 4.6857×10^{-3} m^4, 28.6 GPa, 30 m, and 2400 kg/m^3, respectively. The theoretical buckling load of the beam was 3.0×10^6 N. A finite element model consisted of 300 linear elements (301 nodes) with a uniform length of 0.1 m. For an axial load of 10% of the buckling load, the first two natural frequencies were 1.7859 Hz and 5.9998 Hz. For an intact state of the beam, a constant flexural rigidity EI was assumed for the all elements, while the damaged beam was simulated by reducing EI for specific elements. The distributed damage was simulated by the 10% uniform reduction of flexural rigidity between $x = 13.5$ m and $x = 16.5$ m. Therefore, the exact damage index at the damaged region was $\beta = 1.1111$. Furthermore, the damaged beam had an axial load of 20% of the buckling load and a 15% uniform reduction of mass density. Note that the applied axial load and mass density in the damaged beam were different from those of the undamaged beam. This assumption is quite reasonable, because the applied axial loads and mass density were typically unknown in practice. For instance, any damage event on the deck of a cable-stayed bridge is accompanied by unknown changes in axial forces, because the transverse traffic loads are transferred into axial loads via the inclined cables. It is assumed that an output-only modal testing technique was used to extract the first two mode shapes. The first two frequencies of the damaged beam were 1.8042 Hz and 6.3701 Hz. Note that the frequencies increased when the beam was damaged. This is because the frequencies were affected by changes in local stiffness, mass density, and axial load. The measured mode shapes consisted of only the transverse degrees of freedom with a uniform spacing of 1.5 m at the 19 sensor locations from $x = 0.9$ m to $x = 27.9$ m. Thus a 19×1 mode shape vector for each mode was available before and after a damage event. The first two mode shapes of the undamaged beam are shown in Fig. 7.

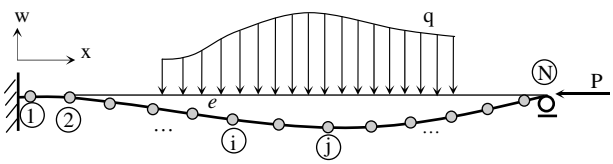

Fig. 6. Axially loaded beam.

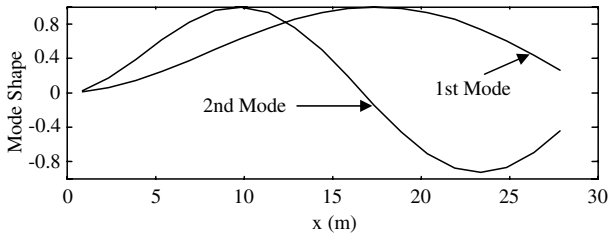

Fig. 7. Mode shapes of the undamaged beam.

To approximate the curvature profiles, the *cubic spline* interpolation method with a uniform interval of 0.0528 m was applied to each mode shape vectors. Applying the central difference formula to the interpolated mode shape vectors (512×1), the curvature profiles vector (19×1) were extracted at the sensor location. The resulting curvature mode shapes for the undamaged beam are shown in Fig. 8. Two end nodes were extrapolated for convenience. The first curvature mode shapes had a singularity near $x = 8$ m, while the second curvature mode shapes had two singularities near $x = 4.4$ m and $x = 16.6$ m. Since those singularities do not overlap, these two mode shapes could be used to construct the wavelet damage index equation (32). The resolution level of the estimated curvature is $j = 5$, because the number of sensors 19 is less than $32 = 2^5$. Therefore, 13 zeros were added to the curvature profiles in order to make a 32×1 vector. Using the Haar wavelet decomposition, the representations of the curvature mode shapes of two modes could be readily obtained. With the aid of Eqs. (30) and (31), a 64×32 matrix $\mathbf{A}$ and a 64×1 vector $\mathbf{b}$ in Eq. (32) were constructed in the Haar domain. For the resulting system of equations, the *pseudo-inverse* solution in Eq. (34) was obtained. Finally, the desired damage indices were reconstructed by Eq. (28). Here, only 19 of 32 damage indices were nonzero, because 13 zeros were added previously to extend the curvatures profile vector. The results are shown in Fig. 9. The localization of damage is successful because a

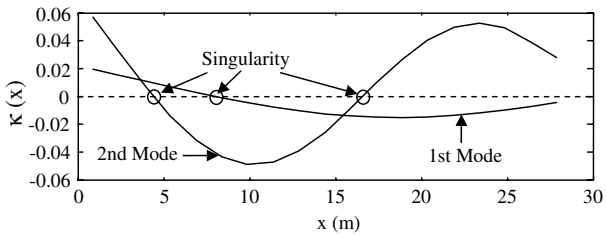

Fig. 8. Curvature mode shapes of the undamaged beam.

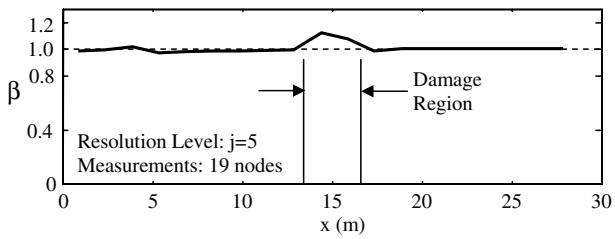

Fig. 9. Estimated damage index using the proposed method ($N = 19$).

distinguishable hump occurred near the damaged region. The identified damage index was $\beta = 1.1074$ at the center of damaged region, and the percentage error of this estimation was only 0.3%. Thus, the severity estimation of damage was also successful. A small hump was also found near the location of the first singularity. This error might be caused by the *pseudo*-inversion, which is an optimum solution. If a scanning laser vibrometer is used, the curvature profile could be determined from a dense deflection profile (up to 512×512 points). Considering the ideal case, the identical solution procedure was repeated with the resolution level $j = 8$ for a 256×1 measured deflection vector. The resolution of damage was improved as shown in Fig. 10.

For the purpose of a comparison study, the MSC and the DI methods were applied to the beam column with the same damage scenario. For the MSC method, the damage index is defined by absolute changes in mode shape curvature:

$$\beta_{\mathrm{MSC}} = |\kappa - \kappa^*| \tag{37}$$

For the 19×1 curvature mode shape of the first mode, the identified damage indices are shown in Fig. 11. The localization of damage was successful, because a clear peak was identified near the damaged region. However, the severity of damage cannot be estimated from the direct inspection of the identified damage index. In fact, the substitution of the damage index equation (3) into Eq. (37) revealed a connection between the proposed damage index and those of the MSC method:

$$\beta_{\mathrm{MSC}} = |\ \kappa(\beta - 1)\ | \tag{38}$$

For the DI method, the damage index of the mth element is defined by

$$\beta_{\mathrm{DI}} = \sum_{i=1}^{n} \frac{\left(\int_m (\kappa_i^*)^2\,\mathrm{d}x + \int_0^L (\kappa_i^*)^2\,\mathrm{d}x\right)\int_0^L (\kappa_i)^2\,\mathrm{d}x}{\left(\int_m (\kappa_i)^2\,\mathrm{d}x + \int_0^L (\kappa_i)^2\,\mathrm{d}x\right)\int_0^L (\kappa_i^*)^2\,\mathrm{d}x} \tag{39}$$

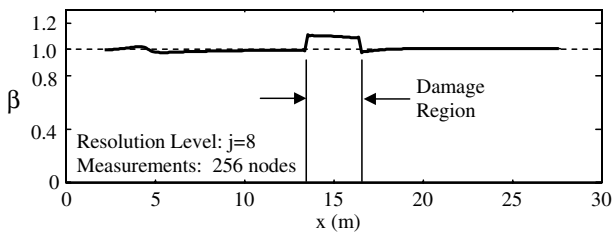

Fig. 10. Estimated damage index using the proposed method ($N = 256$).

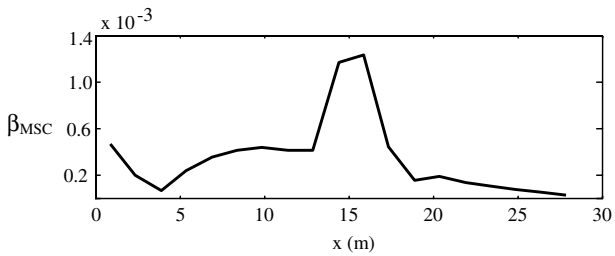

Fig. 11. Estimated damage index using the MSC method.

where the subscript '*i*' denotes the considered mode. For the two interpolated 64×1 curvature profiles, a numerical integration was performed. The estimated damage indices for the two modes are shown in Fig. 12. The clear peak near the simulated damage region was identified. To estimate the severity of damage, a sensitivity-updating algorithm, which is a model-based approach, can be applied (Stubbs and Kim, 1996). However, unlike the proposed wavelet method, the quantitative severity estimation of damage is not attainable by directly inspecting the damage indices.

To investigate the sensitivity of noise, the time history with random noise was considered. For the same damage scenario and measurement grid mesh of 19×1, the displacement time series at the sensor locations were simulated by the modal superposition technique with the first ten lower modes. Here, the required time integrations were carried out in the discrete state-space for unit impulses. The total simulation time, sampling frequency, and damping ratio were 80 s, 500 Hz, and 1.5%, respectively. Thus, the response time histories of the 4×10^4 samples were available at the 19 sensor locations. Next, 19 sets of random noise samples were generated and added to the sets of the response time histories. Here, the noise-to-signal ratio of 5% (a ratio of maximum magnitude of noise to signal) was used. To examine the effect of the number of modal tests, four cases are considered. The modal testing of Case I, II, III, and IV consisted of a total of 5, 10, 30, and 50 simulations, respectively. For example, the modal testing of Case II contained the 10 sets of the 19 noisy time response histories of the 4×10^4 samples for both undamaged and damaged states. For each case of the modal testing scenario, the recently developed time domain decomposition (TDD) technique (Kim et al., 2004) was applied to extract the first two lower mode shapes. Here, the TDD technique is known as an ambient modal analysis method that is efficient and accurate, particularly when there are a large number of sensor locations. After the repeated applications of the TDD technique to each case of modal testing, Case I, II, III, and IV had 5, 10, 30, and 50 sets of the first two lower 19×1 mode shapes for undamaged and damaged conditions, respectively. For the identified damaged mode shapes, the maximum coefficients of variation (a ratio of the standard deviation to the mean value) were 0.0100, 0.0118, 0.0129, and 0.0118 for Case I, II, III, and IV, respectively. Prior to the application of the proposed identification procedures, a set of representative deterministic mode shapes should be computed for each case of modal testing. The representative mode shapes were achieved by averaging the identified mode shapes values at each location. Finally, the proposed method was applied to the resulting averaged mode shapes. The resulting damage indices are shown in Fig. 13. In Case IV, the error of the identified damage index at the damaged region increased by 1.3%. It is seen that the estimated damage indices are degenerated by noise. However, the effect of measurement noise decreased as the number of tests increased. As shown in Fig. 13a, the damage region of Case I could hardly be distinguished from the fictitious peaks that were due to noise. However, the damage regions of Cases II, III, and IV could be distinguished from noise peaks. Therefore, it is concluded that the proposed method requires that clean mode shapes be produced through modal testing. Here, achieving accurate mode shapes relies entirely on the applied modal testing, modal analysis, and data acquisition techniques. Those techniques are continuously evolving by virtue of the challenges posted by other relevant fields.

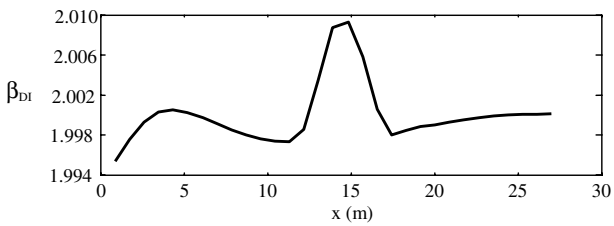

Fig. 12. Estimated damage index using the DI method.

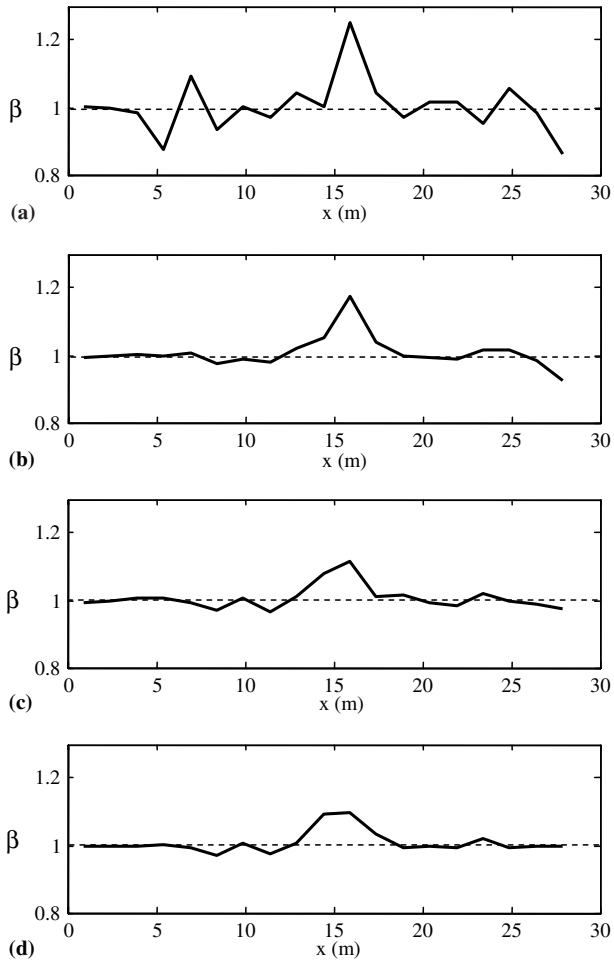

Fig. 13. Estimated damage index for noise data: (a) Case I: 5 modal tests; (b) Case II: 10 modal tests; (c) Case III: 30 modal tests; (d) Case IV: 50 modal tests.

4. Field study

The field data to be used here to evaluate the feasibility of the proposed method are extracted from the study of the impact of inflicted damage on the changes in modal parameters of the I-40 Bridge over the Rio Grande (Farrar et al., 1994). This data set was selected for at least three reasons: First, the data acquisition and processing were performed by an independent and competent team of investigators. Second, the data have received the scrutiny of the technical community. Finally, the data have been used to evaluate several existing damage detection theories.

The north bound and south bound I-40 Bridges over the Rio Grande in Albuquerque, New Mexico, were demolished in 1993 and were replaced by a new bridge. The spans of each bridge consisted of a concrete deck supported by two welded, steel, plate-girders and three steel stringers. The stringers transferred loads from the deck to the plate girders via floor beams located at 6.096 m (20 ft) intervals. Cross-bracing was provided between the floor beams. During the summer of 1993, New Mexico State University and Los Alamos National Laboratory introduced sequential damage to the bridge to simulate fatigue crack growth

in the main plate girder of one of the bridges in order to test various damage identification methods. To simulate fatigue cracking in the bridge, four levels of damage were introduced to the middle span of the north plate girder. Damage was introduced by making various torch cuts in the web and flange of the girder. In this paper, data collected from the mentioned first through fourth levels of damage is used to evaluate the field applicability of the proposed method.

A set of forced vibration tests was performed on the referenced structure (i.e., the structure before any simulated damage was introduced). For each sequential damage scenario, forced vibration tests were repeated. The excitation source was a hydraulic shaker consisting of a 96.526 kN reaction mass supported by three air springs on top of drums filled with sand. The input force was provided by a 9.7861 kN hydraulic actuator bolted under the center of the mass. A random-signal generator was used to produce a 8.8964 kN peak-force uniform random signal over the frequency range 2–12 Hz. An accelerometer mounted on the reaction mass was used to measure the force input-time history. However, this measured excitation signal was not included in the modal analysis. The location of the shaker was the eastern-most span directly above the south plate girder. To measure the output acceleration time histories in the vertical direction and with refined sensor intervals, 11 Endevco 7751-500 accelerometers were mounted on the inside web of the plate girder at mid-height of the plate girder with a nominal spacing of 4.8768 m (16 ft) as shown in Fig. 14. Mode shapes were determined from cross-spectra of the various accelerometer readings relative to accelerometer X3. Each cross-spectrum was obtained using 30 averages with no overlap utilizing a Hanning window. The averaged cross-spectrum had a 0.03125 Hz resolution with 1024 frequency samples. The first three modes were obtained for the undamaged (referenced) structure and four subsequently damaged structures. The first and third modes were bending modes and the second mode was a torsional mode. Note that the mass normalized mode shapes were not available in this forced vibration test because the measured forced input was ignored and the cross-spectra of outputs were used to extract modes. The two flexural mode shapes obtained from the cross-spectra analysis and reported in Farrar et al. (1994) are used in this study.

Since modal data for the undamaged condition of the bridge are available, no attempt is made to build a numerical model of a base-line structure. It is expected that the behavior of the bridge superstructure under investigation here can be modeled accurately by an Euler–Bernoulli beam, since the aspect ratio of the girder to be analyzed is larger than 10. Since only damped modal parameters are available, it is also assumed that a bias in the severity estimation of damage due to the presence of damping is insignificant comparing to the errors due to the placed coarse sensor interval. Since the sensor interval was not uniform, *cubic spline* interpolation with uniform 0.1918 m interval was used to obtain the set of 256×1 mode shape vectors. After applying the central difference formula to the resulting mode shapes, the sets of 11×1 curvature vectors before and after four damage events were extracted at the original sensor location. Thus, sets of the 22×11 system matrices of undamaged (referenced) bridge, $\mathbf{A}$, with full rank (11) were obtained in the Haar domain with the aid of Eqs. (30) and (31). Next, sets of the 11×1 damaged curvature vectors, $\mathbf{b}$, were

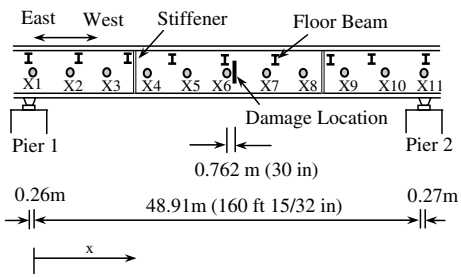

Fig. 14. Sensor location of north plate girder of the Interstate-40 Bridge.

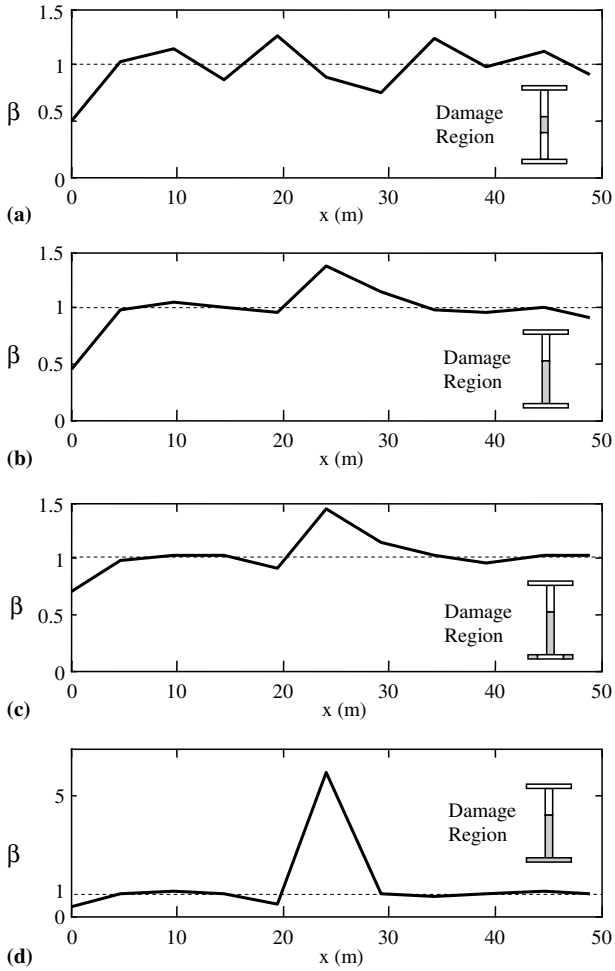

Fig. 15. Estimated damage indices of the Interstate-40 Bridge: (a) damage level I; (b) damage level II; (c) damage level III; (d) damage level IV.

constructed in wavelet space. The resulting set of the over-determined damage equations in Eq. (32) were solved using the previously mentioned *pseudo-inverse* technique in Eq. (34). Finally, sets of the estimated results of the damage index vectors in the Haar domain were reconstructed by Eq. (28). The estimated results with the inflicted damage scenario (gray area) are shown in Fig. 15.

Based on the results, the following three observations can be made: First, the proposed method successfully located the damage in a real structure except the first level of damage. Second, the modal data of the first damage scenario may have poor accuracy. Partial evidence may be inferred from the fact that the overall variation of the estimated damage indices of the first damage scenario is relatively larger compared to the other severe damage scenarios. Third, the proposed method successfully estimated the relative severity of damage, because the estimated damage indices at the location of damage increased as the severity of inflicted damage increased. However, it seems that more accuracy in the severity estimation of damage requires a denser measurement grid. The trade-off between the required costs and desired accuracy should be made.

5. Summary and conclusions

The objective of this study was to introduce a new vibration-based NDE technique. The proposed method made use of the Haar wavelet to resolve some existing deficiencies of the MSC and the DI methods. The deficiencies include the mode selection problem, the singularity problem, the axial force consideration, and the estimation of the absolute severity of damage. In order to achieve this goal, a damage mechanism that inherently contains a singularity problem was given. To resolve the singularity problem, the fundamentals of the multi-resolution wavelet analysis were introduced in detail. Using the Haar wavelet transformation, the damage mechanism gave a set of linear algebraic equations. With the aid of singular value decomposition, the singularities in the damage mechanism were discarded. Finally, the desired damage index was reconstructed using the *pseudo*-inverse solution. Next, the performance of the proposed method was compared with two existing NDE methods for an axially loaded beam without any special knowledge about mass density and an applied axial force. Finally, the effect of random noise on the performance was simply examined.

Based on the results of the numerical experiments, the following five findings can be asserted: First, the proposed method provided a single representative damage index using more than one mode. Thus, the uncertainty of mode selection that exists in earlier attempts was resolved. Second, the proposed method made use of the singular value decomposition of the system of equations in a wavelet domain. Thus, the singularity problem near the inflection points can be resolved. Third, the proposed method did not require any special knowledge about mass density, applied axial force, or foundation stiffness. The reason is that such structural environments do not affect the internal moments. Thus, the proposed method could be applied to a pre-stressed or post-tensioned beam, a deck of cable-stayed bridges, etc. Fourth, the estimated damage index could be interpreted as a ratio of the undamaged flexural rigidity to the damaged flexural rigidity. Therefore, the location and the severity of damage could be directly recognized by the inspection of the resulting damage indicator. Finally, starting from Eq. (1), the proposed method could be easily extended to other classes of structures, because the proposed approach is based on the well-established context of elasticity.

Despite its strong features, the proposed method still has at least the following two weaknesses: First, a dense measurement of grid was needed for good accuracy. For this problem, the aforementioned scanning laser vibrometer seems to be a unique solution at this time. Second, the accurate extraction of the mode shapes was considered to be a prerequisite. This requirement may be overcome by advanced modal testing, modal analysis techniques, and novel data acquisition devices.

References

Berman, A., Flannelly, W.G., 1971. Theory of incomplete models of dynamic structures. AIAA Journal 9 (8), 1481–1487.

Blevins, R.D., 1979. Formulas for Natural Frequency and Mode Shape. D. Van Nostrand Reinhold Company, London.

Cawley, P., Adams, A.D., 1979. The location of defects in structures from measurements of natural frequencies. Journal of Strain Analysis 14 (2), 49–57.

Doebling, S.W., Peterson, L.D., Alvin, K.F., 1996. Estimation of reciprocal residual flexibility from experimental modal data. AIAA Journal 34 (8), 1678–1685.

Douka, E., Loutridis, S., Trochidis, A., 2003. Crack identification in beams using wavelet analysis. International Journal of Solids and Structures 40, 3557–3569.

Farrar, C.R., Jauregui, D.A., 1998. Comparative study of damage identification algorithms applied to a bridge: I experiment. Smart Materials and Structures 7, 704–719.

Farrar, C.R., Baker, W.E., Bell, T.M., Cone, K.M., Darling, T.W., Duffey, T.A., Eklund, A., Migliori, A., 1994. Dynamic characterization and damage detection in the I-40 Bridge over the Rio Grande. Report No. LA-12767-MS, Los Alamos National Laboratory, Los Alamos, NM.

Gentile, A., Messina, A., 2003. On the continuous wavelet transforms applied to discrete vibrational data for detecting open cracks in damaged beams. International Journal of Solids and Structures 40, 295–315.

Golub, G.H., Van Loan, C.F., 1996. Matrix Computations, fourth ed. The Johns Hopkins University Press, Baltimore, MD.

Hong, J.-C., Kim, Y.Y., Lee, H.C., Lee, Y.W., 2002. Damage detection using the Lipschitz exponent estimated by the wavelet transform: applications to vibration modes of a beam. International Journal of Solids and Structures 39, 1803–1816.

Kim, B.H., Stubbs, N., Sikorsky, C., 2002. Local damage detection using incomplete modal data. In: Proceedings of the 20th International Modal Analysis Conference, Los Angeles, CA, pp. 435–441.

Kim, B.H., Stubbs, N., Park, T., 2004. A new method to extract modal parameters using output-only responses. Journal of Sound and Vibration 282, 215–230.

Loutridis, S., Douka, E., Trochidis, A., 2004. Crack identification in double-cracked beams using wavelet analysis. Journal of Sound and Vibration 277, 1025–1039.

Mallat, S., 1998. A wavelet tour of signal processing. Academic Press, London.

Messina, A., 2004. Detecting damage in beams through digital differentiator filters and continuous wavelet transforms. Journal of Sound and Vibration 272, 385–412.

Pai, P.F., Young, L.G., 2001. Damage detection of beams using operational deflection shapes. International Journal of Solids and Structures 38, 3161–3192.

Pandey, A.K., Biswas, M., Samman, M.M., 1991. Damage detection from changes in curvature mode shapes. Journal of Sound and Vibration 145 (2), 321–332.

Pandey, A.K., Biswas, M., 1994. Damage detection in structures using changes in flexibility. Journal of Sound and Vibration 169 (1), 3–17.

Shao, X., Ma, C., 2003. A general approach to derivative calculation using wavelet transform. Chemometrics and Intelligent Laboratory Systems 69, 157–165.

Stollnitz, E.J., DeRose, T.D., Salesin, D.H., 1995. Wavelets for computer graphics: a primer. IEEE Computer Graphics and Applications 15 (3), 76–84.

Stubbs, N., Kim, J.T., 1996. Damage localization in structures without baseline modal parameters. AIAA Journal 34 (8), 1644–1649.

Stubbs, N., Kim, J.T., Farrar, C.R., 1995. Field verification of a nondestructive damage localization and severity estimation algorithm. In: Proceedings of the 13th International Modal Analysis Conference, Nashville, Tennessee, vol. 1, pp. 210–218.

Timoshenko, S., 1928. Vibration Problems in Engineering. D. Van Nostrand Company, Inc., London.

Wahab, M.M.A., Roeck, G.D., 1999. Damage detection in bridges using modal curvature: application to a real damage scenario. Journal of Sound and Vibration 226 (2), 217–235.

Wang, Q., Deng, X., 1999. Damage detection with spatial wavelets. International Journal of Solids and Structures 36, 3443–3468.